Check for updates

Ce³⁺-enriched spherical porous ceria with an enhanced oxygen storage capacity†

Ayano Taniguchi,[a] Yoshitaka Kumabe,[a] Kai Kan, [ID] [abc] Masataka Ohtani [ID] *[abc] and Kazuya Kobiro [ID] *[abc]

Porous ceria was obtained using a unique solvothermal reaction in acetonitrile, applying high temperature and pressure. The resulting material comprised homogeneous and monodisperse spheres and exhibited an extremely large surface area of 152 m² g⁻¹. From catalytic performance evaluation by vapor- and liquid-phase reactions, the synthesized porous ceria showed superior and different reaction activity compared with commercial CeO_2. To examine the origin of the reaction activity of the present porous ceria, synchrotron hard X-ray photoelectron spectroscopy (HAXPES) measurements were carried out. The systematic study of HAXPES measurements revealed that the obtained porous ceria with the present solvothermal method contained a very high concentration of Ce^{3+}. Moreover, O_2-pulse adsorption analyses demonstrated a significant oxygen adsorption capacity exceeding 268 μmol-O g⁻¹ at 400 °C owing to its high contents of Ce^{3+} species.

Introduction

Ceria is well known as a catalyst or a catalyst support with applications in many different reactions.[1] Especially in the case of oxidation reactions, the presence of Ce^{3+} ions (ascribed to defects in CeO_2 crystals) and the Ce^{3+}/Ce^{4+} redox cycle are believed to be important in terms of establishing the catalytic effects of ceria.[2–4] Additionally, the oxygen storage capacity (OSC) of this material is also directly affected by oxygen defects due to the presence of neighbouring Ce^{3+},[5] and so there has been a significant effort to develop methods of synthesizing ceria with a high Ce^{3+} content. However, it is challenging to obtain ceria with a high proportion of stable Ce^{3+} such that this lower valence state is maintained over time, because Ce^{3+} is easily oxidized to the more thermodynamically stable Ce^{4+} state in air.[6,7]

One preparation method that has been successfully demonstrated is the reduction of CeO_2 by Ce metal at high temperatures in the vicinity of 1500 °C,[8] although sintering of the ceria particles inevitably leads to a small surface area. The reduction of CeO_2 nanosheets, which have relatively large surface areas, is an alternative approach, but involves a more complex two-step process.[9] Mesoporous CeO_2 with an increased OSC has also been obtained using hard templates such as SBA-15, although the template must subsequently be removed.[10] There are several reports related on high OSC values of un-doped CeO_2 determined by several different methods, for example 156 μmol-O_2 g⁻¹ (determined by thermogravimetry at 200 °C),[11] 461 μmol-O g⁻¹ (determined by thermogravimetry at 300 °C)[12] and 554 μmol-O g⁻¹ (determined by CO-pulse at 400 °C).[13] Finally, the doping of CeO_2 with different elements, including Si, Ti, Y, Zr, La and Cr, has been employed as a means of introducing stable defects based on lattice strain into ceria crystals to improve the OSC.[14–16]

Recently, Hao *et al.* reported a unique procedure yielding ceria nanocrystals with a high concentration of Ce^{3+} based on an improved hydrothermal method.[17] Their work showed that smaller nanocrystals contained higher levels of Ce^{3+} defects and that these defects were primarily situated at the surfaces of the nanoparticles. Additionally, the proportion of defects (that is, unsaturated coordination sites) was found to increase as the particle size decreased, and these defects were primarily present at the corners and edges of the nanocrystals.

As can be seen from the above examples, the concentration of Ce^{3+} in ceria is highly dependent on both the synthetic methodology and the reaction environment. Our group previously established a simple one-step solvothermal method for the preparation of submicron-sized, porous spheres made of oxides such as SiO_2, TiO_2, ZrO_2 and CeO_2 as well as composites of these oxides. These materials exhibited large surface areas and unique concave-convex surface structures on the nanoscale.[18–20] These oxides were termed micro/mesoporously architected roundly integrated metal oxides (MARIMOs). In

[a]School of Environmental Science and Engineering, Kochi University of Technology, 185 Miyanokuchi, Tosayamada, Kami, Kochi 782-8502, Japan. E-mail: ohtani. masataka@kochi-tech.ac.jp; kobiro.kazuya@kochi-tech.ac.jp

[b]Laboratory for Structural Nanochemistry, Kochi University of Technology, 185 Miyanokuchi, Tosayamada, Kami, Kochi 782-8502, Japan

[c]Research Center for Molecular Design, Kochi University of Technology, 185 Miyanokuchi, Tosayamada, Kami, Kochi 782-8502, Japan

prior work, an Au metal nanoparticle catalyst deposited on a TiO$_2$ MARIMO substrate showed excellent resistance to temperature stress during the CO oxidation reaction, without sintering of the Au nanoparticles.[21] The submicron spherical porous morphology of these MARIMOs also favors heterogeneous catalysis applications, because these spheres are more readily dispersed than standard nanoparticles, which tend to agglomerate.

We considered that a solvothermal reaction performed under a reductive atmosphere over a very short time span would produce an appreciable concentration of Ce^{3+} defects in ceria nanocrystals, based on previous syntheses of metal oxide nanoparticles.[22–24] Therefore, in the present work, we applied this technique to produce a ceria MARIMO comprising nanocrystals rich in Ce^{3+} by optimizing the solvothermal reaction conditions (including the solvent, additives, temperature and time). The unique properties of the resulting ceria MARIMO were examined and are discussed herein.

Experimental details

Materials

Methanol, acetonitrile, toluene, formic acid, acetic acid, benzoic acid, phthalic acid, ethylene glycol, diethylene glycol, cerium(III) nitrate hexahydrate (Ce(NO$_3$)$_3$·6H$_2$O), potassium chloroplatinate(II) (K$_2$PtCl$_4$) and aniline were purchased from FUJIFILM Wako Pure Chemical Corporation. Triethylene glycol and n-tridecane was purchased from Tokyo Chemical Industry Co., Ltd. Benzyl alcohol was purchased from Nacalai Tesque Inc. Reference ceria catalyst, JRC-CEO-5, was received from Daiichi Kigenso Kagaku Kogyo Co., Ltd. All chemicals were used as received without further purification.

Preparation of CeO$_2$-AN-tEG

The ceria MARIMO (CeO$_2$-AN-tEG) was synthesized according to a previously developed procedure for the preparation of a TiO$_2$ MARIMO.[18] An acetonitrile solution (140 mL) including Ce(NO$_3$)$_3$·6H$_2$O (6.08 g, 14.0 mmol) and triethylene glycol (66.7 g, 444 mmol) was transferred to an SUS316 autoclave 500 mL volume high pressure micro reactor (MMJ-500, OM Labtech Co., Ltd. Available maximum temperature and pressure are 300 °C and 20 MPa, respectively.). The reactor was heated to 300 °C at a rate of 5.4 °C min^{-1}. The temperature was kept at 300 °C for 10 min. Then, the reactor was cooled to room temperature to quench the reaction. The obtained product was centrifuged, washed with methanol, and then dried under vacuum for overnight at room temperature to give a powder. Preparation methods of other samples are described in ESI.†

Catalyst preparation

CeO$_2$-AN-tEG supported 1 wt% Pt nanoparticles catalyst was prepared by using a standard precipitation–deposition method.[25] Ceria support (CeO$_2$-AN-tEG, 1 g) was dispersed in 100 mL of reverse osmosis water. K$_2$PtCl$_4$ aqueous solution (5.18 mL, 10.0 mmol L^{-1}) was added to the suspension with vigorous stirring at room temperature. After 2 h, the mixture was

centrifuged to collect precipitate. The precipitate was washed with reverse osmosis water, and centrifuged. The obtained product was dried under vacuum overnight (*ca.* 15 h), and calcined in air at 300 °C for 4 h to get a powder, namely, 1 wt% Pt/CeO$_2$-AN-tEG catalyst. 1 wt% Pt/JRC-CEO-5 catalyst was prepared in the similar procedure.

Characterization

Transmission electron microscope (TEM) and scanning electron microscope (SEM) images were taken on a JEOL JEM-2100F microscope and a Hitachi SU8020 microscope, respectively. Energy-dispersive X-ray spectroscopy (EDX) were performed on an Oxford INCA X-Max 80 EDX spectrometer equipped on the TEM instrument. X-ray diffraction (XRD) patterns were measured using a Rigaku SmartLab diffractometer with graphite-monochromatized Cu-Kα radiation (X-ray wavelength: 1.5418 Å). Nitrogen adsorption/desorption isotherm measurements were carried out using a BEL BELSORP Mini II. Specific surface area and average pore size were calculated by the Brunauer–Emmett–Teller (BET) method and the Barrett–Joyner–Halenda (BJH) calculation, respectively. Thermogravimetry (TG) was carried out using a HITACHI STA7200RV. Hard X-ray photoelectron spectroscopy (HAXPES) spectra were measured at the SPring-8 BL15XU beam line. CO oxidation test, O$_2$-pulse absorption measurement and H$_2$ temperature-programmed reduction (H$_2$-TPR) measurement were carried out using a MicrotracBEL BELCAT II.

Nitrogen adsorption/desorption isotherm

Before performing measurement, CeO$_2$ (as-synthesized CeO$_2$-AN-tEG and JRC-CEO-5) were pre-treated by vacuum heating at 250 °C for 4 h to remove organic residue and absorbed moisture on surface.

TG analysis

TG of CeO$_2$-AN-tEG was performed to investigate burning or decomposing temperature of organic residue in the product and its amount. As-synthesized CeO$_2$-AN-tEG (*ca.* 5 mg) was heated up to 800 °C from 25 °C ramp rate of 2 °C min^{-1} in air flow (100 mL min^{-1}). Similarly, calcined CeO$_2$-AN-tEG (300 °C, 1 h, in air) was also analysed to check amounts of organic residues.

Analysis of HAXPES spectra

Peak fitting of Ce 3d HAXPES spectra was carried out by using KolXPD software. A background signal was fitted using well known Shirley method. All multiple peaks were fitted as Gaussian/Lorentzian peak. The multiple peaks were fitted to 10 peaks correspond to the spin–orbit split 3d$_{5/2}$ (= v^0, v, v', v'', v''') and 3d$_{3/2}$ (= u^0, u, u', u'', u'''). The spin–orbit splitting was fixed to 18.4 eV. The peak intensity ratio of 3d$_{5/2}$/3d$_{3/2}$ was fixed to 1.5. The peaks of v^0, v', u^0 and u' and v, v'', v''', u, u'' and u''' correspond to the Ce(III) and Ce(IV) species, respectively. The Ce^{3+} concentration was calculated by following equation:

$$Ce^{3+}(\%) =$$

$$\frac{A_{v^0} + A_{v'} + A_{u^0} + A_{u'}}{A_{v^0} + A_v + A_{v'} + A_{v''} + A_{v'''} + A_{u^0} + A_u + A_{u'} + A_{u''} + A_{u'''}}$$

Here, A_i shows the peak area of the i peak.

Vapor-phase catalytic reactions

Before performing CO oxidation, CeO_2 (as-synthesized CeO_2-AN-tEG and JRC-CEO-5) were calcined at 300 °C for 1 h in air to remove organic residue. Calcination temperature was decided by TG profile of as-synthesized CeO_2-AN-tEG (Fig. S1†). The calcined CeO_2 (50 mg) or prepared Pt/CeO_2 catalyst (30 mg) was pre-treated at 300 °C for 60 min in O_2 flow at a flow rate of 30 sccm (100 vol%) before reaction. Then, CO oxidation was performed using CO (4 sccm, 13 vol%), O_2 (2 sccm, 7 vol%) and Ar (24 sccm, 80 vol%) in the temperature range of 150–350 °C for the test of CeO_2 or in a temperature range of 50–300 °C for the test of Pt/CeO_2. The outlet gas was analyzed by a GL Science GC-3200 gas chromatograph with an active carbon column and a thermal conductivity detector (TCD) using Ar as a carrier gas.

Liquid-phase catalytic reaction

To a solution of benzyl alcohol (517 μL, 5.00 mmol), aniline (912 μL, 10.0 mmol) and n-tridecane (608 μL, 2.50 mmol) as an internal standard for GC in 10.0 mL toluene was added as-synthesized CeO_2-AN-tEG (250 mg) under O_2 atmosphere. The mixture was heated at 60 °C. Then, an aliquot amount of reaction mixture was withdrawn by syringe through a membrane filter. The product distribution was determined by a Shimadzu GC-17A gas chromatograph equipped with an Agilent Technologies DB-1 column (30 m × 0.25 mm × 0.25 μm), flame ionization detector (FID), and helium as a carrier gas. Only a negligible amount of benzaldehyde was detected during the reaction. Similarly, the reaction was also performed in the cases of JRC-CEO-5 and calcined CeO_2-AN-tEG (300 °C, 1 h, in air) as catalysts. In pre-treatment, as-synthesized CeO_2-AN-tEG was stirred in toluene (7.00 mL) at 60 °C for 48 h under O_2 atmosphere prior to an addition of a mixture of a toluene solution (3.00 mL) of aniline (10.0 mmol), benzyl alcohol (5.00 mmol) and n-tridecane (2.50 mmol, internal standard for GC analysis). Reaction time was recorded after 48 h in the case of pre-treatment in Fig. S6a.†

H_2-TPR

Before H_2-TPR measurement, CeO_2 (as-synthesized CeO_2-AN-tEG and JRC-CEO-5) were pre-treated for 60 min each at 300 °C and 50 °C in 20 vol% O_2/Ar flow at flow rate of 30 sccm to remove organic residue and oxidation of CeO_2. Then, H_2-TPR measurement was performed using 6 vol% H_2/Ar (30 sccm) in
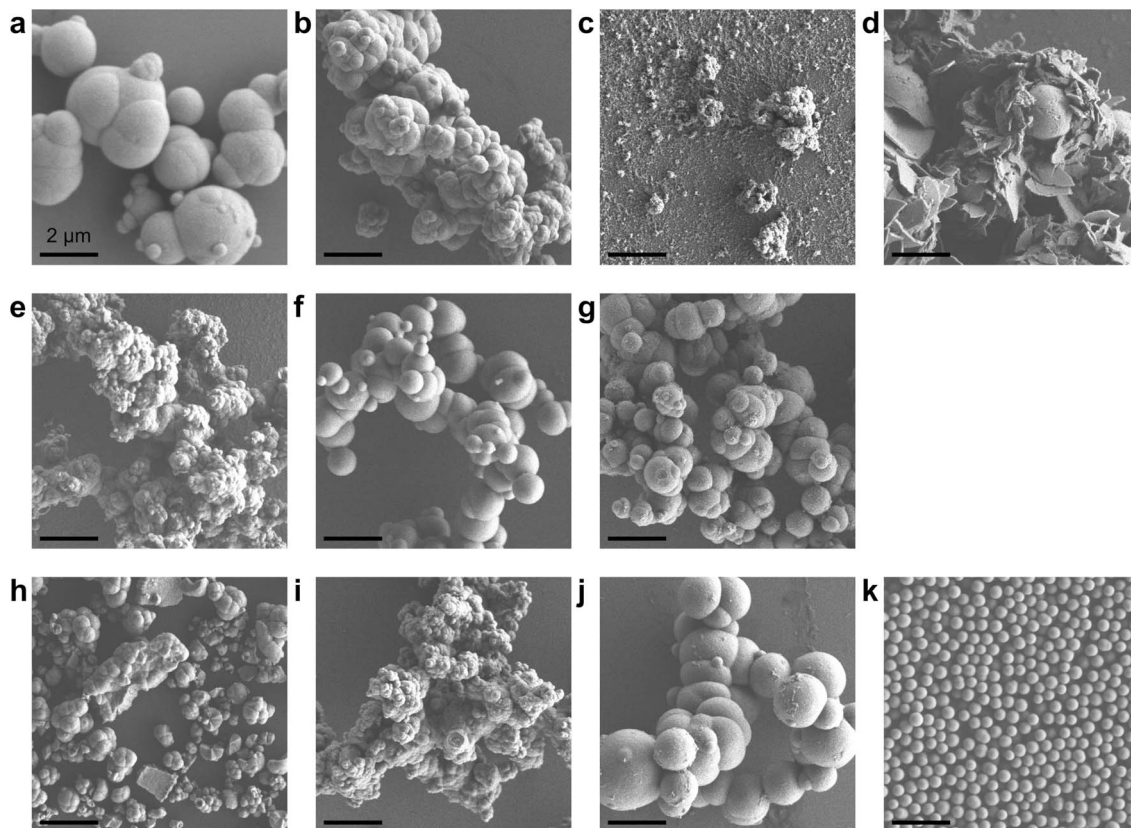

Fig. 1   SEM images of the prepared ceria (scale bar: 2 μm). (a) CeO_2-ME-FA, (b) CeO_2-ME-AA, (c) CeO_2-ME-BA, (d) CeO_2-ME-PA, (e) CeO_2-ME-EG, (f) CeO_2-ME-dEG, (g) CeO_2-ME-tEG, (h) CeO_2-AN, (i) CeO_2-AN-EG, (j) CeO_2-AN-dEG and (k) CeO_2-AN-tEG, where short abbreviations ME, FA, AA, BA, PA, EG, dEG, tEG and AN represent methanol, formic acid, acetic acid, benzoic acid, o-phthalic acid, ethylene glycol, diethylene glycol, triethylene glycol and acetonitrile, respectively.

the temperature range of 50–700 °C (ramp rate was 10 °C min^{-1}). The outlet gas was analyzed by a BELCAT II equipped with a TCD using Ar as a carrier gas.

Cyclic O$_2$-pulse adsorption

Prior to pulse measurement, CeO$_2$ (as-synthesized CeO$_2$-AN-tEG or JRC-CEO-5) was calcined at 300 or 400 °C for 60 min in air to remove organic residue, and the calcined CeO$_2$ (50 mg) was pre-treated at 200 or 400 °C for 60 min in 10 vol% H$_2$/He (30 sccm). Then, O$_2$-pulse adsorption measurement was performed using 10 vol% O$_2$/He (30 sccm) at 200 or 400 °C. These procedures were repeated several times. The outlet gas was analyzed by BELCAT II equipped with a TCD using Ar as a carrier gas.

Results and discussion

Synthesis of porous CeO$_2$ spheres

Porous CeO$_2$ were synthesized by simple procedure involved heating a mixture of Ce(NO$_3$)$_3$·6H$_2$O and an additive in a solvent to 300 °C (Table S1†). The particular combination of solvent and additive was found to modify the morphology of the product (Fig. 1). Interestingly, a combination of methanol and formic acid or acetic acid, which was previously employed in the synthesis of the TiO$_2$ MARIMO,[18,26] did not yield a monodisperse CeO$_2$ MARIMO. Rather, irregularly aggregated porous spheres having a cubic crystal phase were obtained (Fig. 1a, b and 2a, b). Using benzoic acid as an additive, primary CeO$_2$ nanoparticles with a cubic crystal phase were generated but did not aggregate to form secondary structures (Fig. 1c and 2c). Moreover, the usage of phthalic acid resulted in thin flakes (Fig. 1d) that generated an XRD pattern suggesting a crystal phase different from that of cubic ceria (Fig. 2d). Additional trials were performed using oxyethylene compounds as additives because these are well known chelating reagents based on the coordination of oxygen atoms to the central metal ions of metal salts.[27,28] These trials produced cubic CeO$_2$ aggregates with improved porous spherical morphologies in accordance with the number of oxyethylene units (Fig. 1e–g and 2e–g). However, the products were not monodispersed but rather showed significant aggregation of the spheres.

Subsequently, we selected acetonitrile as an alternative solvent because it is a representative polar solvent being capable of dissolving a number of different inorganic compounds.[29] In trials without the use of additives, non-uniform aggregates were obtained (Fig. 1h), while improved morphologies were observed in accordance with the number of oxyethylene units in additives (Fig. 1i–k). Surprisingly, the use of triethylene glycol resulted in a completely monodisperse and almost perfectly spherical morphology (sample CeO$_2$-AN-tEG, Fig. 1k and 3). Such beautiful spherical morphology can be derived from minimizing contact surface area with outer atmosphere (solvent) in the reaction, as can be seen in emulsification polymerization, which could be one reason.[26] This product had a crystallite size of 3.3 nm as determined using Scherrer's equation in conjunction with the XRD pattern for the material (Fig. 2k). The diameters of the spheres were determined to be 440 ± 40 nm
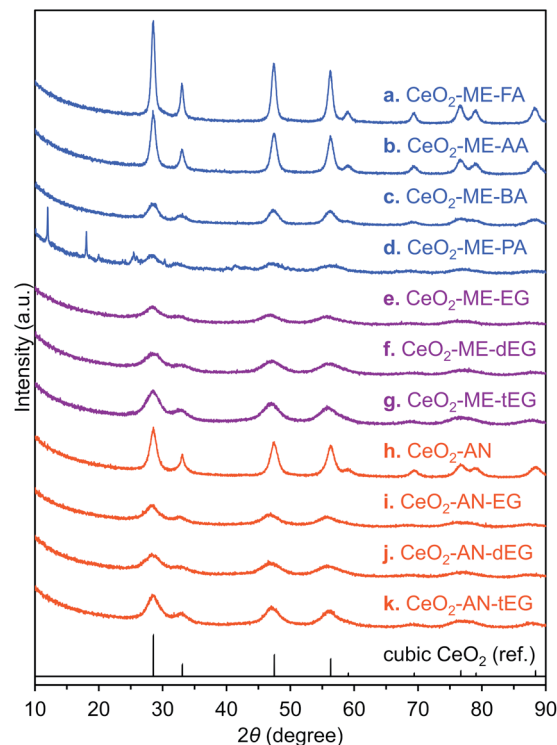

Fig. 2 XRD patterns of ceria porous spheres. (a) CeO$_2$-ME-FA, (b) CeO$_2$-ME-AA, (c) CeO$_2$-ME-BA, (d) CeO$_2$-ME-PA, (e) CeO$_2$-ME-EG, (f) CeO$_2$-ME-dEG, (g) CeO$_2$-ME-tEG, (h) CeO$_2$-AN, (i) CeO$_2$-AN-EG, (j) CeO$_2$-AN-dEG and (k) CeO$_2$-AN-tEG. Black line represents reference XRD pattern of cubic CeO$_2$.

based on SEM images (Fig. 1k). Comparing to XRD patterns of four samples CeO$_2$-AN, CeO$_2$-AN-EG, CeO$_2$-AN-dEG and CeO$_2$-AN-tEG, crystallinity of CeO$_2$-AN was significantly higher than that of other three samples. Therefore, it is considered that oxyethylene compounds suppress crystal growth of the primary particles by chelate effect to precursor Ce ion and/or generated primary particles. Furthermore, judging from the monodisperse state of sample CeO$_2$-AN-tEG, it was suggested that the oxyethylene compounds suppressed the aggregation of secondary particles, too. Thus, triethylene glycol performed the best additive in the three oxyethylene compounds, which can be ascribed to effective coordination through three oxyethylene units. The BET specific surface area was large at 152 m^2 g^{-1} (Fig. S2a†) while the BJH pore size distribution peak was less
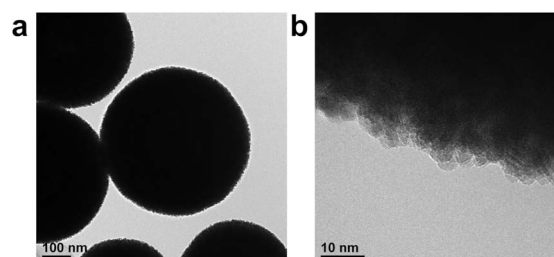

Fig. 3 Morphology of porous ceria sphere (CeO$_2$-AN-tEG). (a) TEM image and (b) high resolution TEM image.

than 2.43 nm (the lower limit of the instrument, Fig. S2b†). Concave-convex surface structures on the nanoscale are clearly evident in TEM images of the MARIMO surface (Fig. 3b), which would be expected to provide a heat-tolerant catalyst support based on previous work.[21,30] Judging from these physical properties, it was anticipated that this CeO_2 MARIMO (CeO_2-AN-tEG) could potentially serve as a high-performance catalyst support for metal nanoparticle catalysts.

Evaluation of the catalytic performance

The performance of the CeO_2-AN-tEG as a catalyst or a catalyst support was examined by performing a highly exothermic CO oxidation reaction as a probe reaction. In these trials, a JRC-CEO-5 (Japan Reference Catalyst) standard with a specific surface area of 92.0 m^2 g^{-1} and an average crystallite size of 9.9 nm was employed as a reference material.[31] The TEM image in Fig. S3b† clearly shows several Pt nanoparticles on the JRC-CEO-5 catalyst, while no Pt particles are evident in the case of the Pt/CeO_2-AN-tEG catalyst (Fig. S3a†). However, based on EDX analyses, the JRC-CEO-5 and CeO_2-AN-tEG contained 1.1 and 0.9 wt% Pt, respectively, thus, indicating that the Pt nanoparticles would be highly dispersed on the CeO_2-AN-tEG.

The catalytic CO oxidation reaction was examined using both the porous ceria spheres and the reference ceria, both with Pt nanoparticles. Fig. 4a plots the CO_2 yields as functions of reaction temperature. As expected, the Pt/CeO_2-AN-tEG catalyst exhibited superior low temperature catalytic activity. Although the oxidation reaction started at 150 °C in the case of the Pt/JRC-CEO-5, a substantially lower onset temperature of 50 °C was observed when using the Pt/CeO_2-AN-tEG. Notably, the CO_2 yield reached almost 100% at 100 °C with the latter material, at which temperature the Pt/JRC-CEO-5 reaction had just begun. The higher oxidation ability of Pt/CeO_2-AN-tEG catalyst than that of reference Pt/JRC-CEO-5 can be explained as follows: it is well known that the ceria–metal interface activates oxygen in CO oxidation reactions at the ceria–metal interface with smooth oxygen transfer between Pt and ceria support.[32] The large surface area and convex-concave surface structure would

disperse Pt particles well and serve larger amounts of ceria–metal interface.

In trials using the CeO_2-AN-tEG without Pt during the CO oxidation reaction, the reaction was found to start at 225 °C with 90% conversion at 250 °C, as can be seen in Fig. 4b. In contrast, the reaction started at 250 °C when using the JRC-CEO-5 and 86% conversion was achieved at 300 °C. Thus, the bare CeO_2-AN-tEG exhibited higher CO conversion as well as superior low temperature activity. As discussed above, the higher specific surface area of the CeO_2-AN-tEG (127 m^2 g^{-1}: after calcined at 300 °C for 1 h in air) compared with that of the JRC-CEO-5 (87.6 m^2 g^{-1}: after calcined at 300 °C for 1 h in air) may be one reason for its superior catalytic CO conversion properties. However, it is still difficult to fully explain the reason for the higher catalytic activity of this material at low temperatures, unless differences in another factor of the porous ceria are taken into account. Evaluation in other catalytic reaction should be performed to understand the superior low temperature catalytic activity of CeO_2-AN-tEG.

In other trials, an unexpected difference in reactivity was observed in liquid-phase reactions. CeO_2 is known to act as a redox catalyst in liquid-phase reactions and so the CeO_2-AN-tEG was applied to the catalytic oxidation reaction of benzyl alcohol to benzaldehyde under O_2. This reaction was followed by conversion to *N*-benzylideneaniline *via* condensation with aniline *in situ* as shown in Fig. S4.†[33] In this reaction, the oxidation of benzyl alcohol is promoted by redox sites on the ceria, while the subsequent condensation reaction between benzaldehyde and aniline is facilitated by the Lewis acid sites on the material.[34–37] The associated reaction profiles are presented in Fig. 4c. Based on the specific surface areas of the porous ceria and of the reference compound (JRC-CEO-5), it was predicted that the porous ceria would be more active. However, the reaction profile using CeO_2-AN-tEG was found to be very different from that of JRC-CEO-5, such that the former required a long induction period (*ca.* 48 h) to initiate the reaction. Thus, it seems that other factors, such as structure, electronic state, high oxygen diffusivity and lower activation energy by high lattice strain, relate to catalytic activity of CeO_2, which could
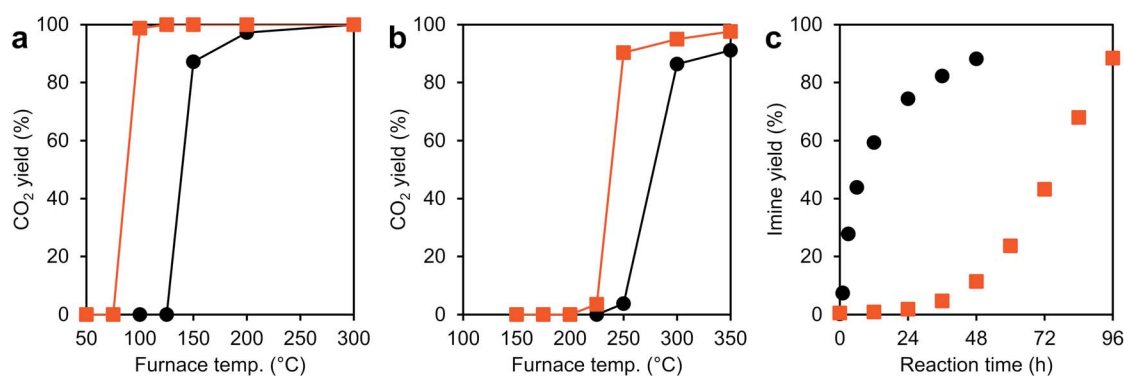

Fig. 4 Results of catalytic reactions with Pt/CeO_2 and CeO_2 catalysts. (a) The vapor-phase CO oxidation reaction catalyzed by Pt/CeO_2-AN-tEG (red) and Pt/JRC-CEO-5 (black). (b) The vapor-phase CO oxidation reaction catalyzed by CeO_2-AN-tEG (red) and JRC-CEO-5 (black). (c) The liquid-phase oxidation reaction of benzyl alcohol catalyzed by CeO_2-AN-tEG (red) and JRC-CEO-5 (black) followed by condensation with aniline.

compensate smaller specific surface area *in the case of this liquid-phase reaction*.

HAXPES analysis

To establish the origin of the unexpected catalytic activity of this material, the valences of the Ce ions in the ceria were assessed using HAXPES at the SPring-8 facility (Fig. S5†), where photoelectrons released from *ca.* 7 nm depth from the particle surface can be detected because of strong synchrotron X-ray (5949 eV) at the SPring-8 synchrotron radiation facility.[38] Judging from the primary particle size of the CeO_2 MARIMOs (*ca.* 4 nm), entire inside electronic structure can be detected. This was done because the concentration of point defects in CeO_2, which directly affects oxygen uptake/release efficiencies, is an important factor controlling catalytic activity. The peak fitting curves (Fig. 5) clearly demonstrates that the reference ceria JRC-CEO-5 generated small peaks at the positions attributed to Ce^{3+} (880.9, 885.2, 899.1 and 903.4 eV).[39] However, the CeO_2-AN-tEG prepared by the solvothermal reaction in acetonitrile exhibited obviously large peaks at these positions.[7,40–42] These results clearly demonstrate that the JRC-CEO-5 contained exclusively Ce^{4+} while the CeO_2-AN-tEG had a high proportion of Ce^{3+}, where concentration of Ce^{3+} in JRC-CEO-5 was determined to 22.5 at% by peak fitting of HAXPES profiles. On the other hand, Ce^{3+} proportion of CeO_2-AN-tEG turned out extremely high, to be 57.4 at%. Hao *et al.* reported that the amount of Ce^{3+} in CeO_2 nano-sized crystals increased as the CeO_2 particle size
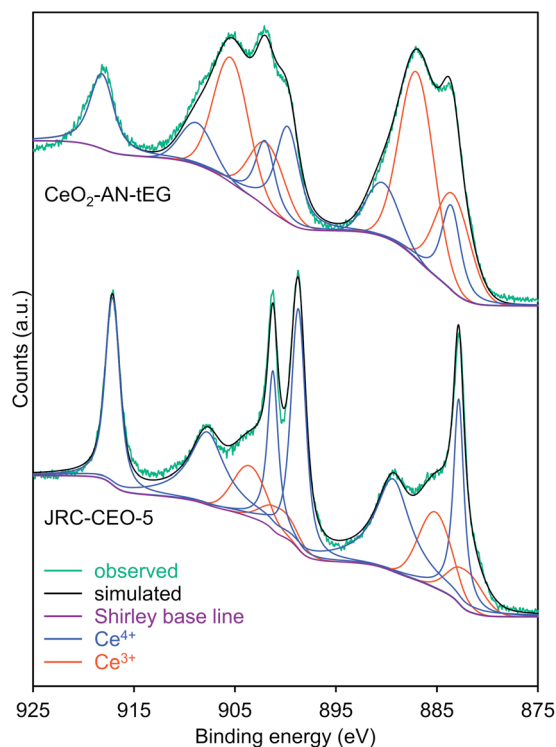

Fig. 5 Ce 3d HAXPES spectra and peak fitting curves of CeO_2-AN-tEG and JRC-CEO-5. Observed (green), Shirley base line (violet), deconvolution peaks of Ce^{4+} (blue), deconvolution peaks of Ce^{3+} (red) and simulated curve (black).

decreased.[17] The crystallite size in the CeO_2-AN-tEG was estimated to be 3.3 nm and so was comparable to the value previously reported for CeO_2 nanocrystals (5.4 nm) including high proportions of Ce^{3+}.[17] Thus, the small crystallite size of the CeO_2-AN-tEG could be one reason for the existence of an appreciable amount of Ce^{3+} in the CeO_2-AN-tEG nanocrystals.

The Ce^{3+} in the original $Ce(NO_3)_3\cdot 6H_2O$ would be expected to be oxidized to Ce^{4+} during the solvothermal reaction that yielded CeO_2. However, the reductive nature of the solvothermal system could be another reason for the large amount of Ce^{3+} in the porous CeO_2 spheres. That is, the hydroxy groups of the triethylene glycol could have acted as reducing agents, while the acetonitrile would have no oxidation ability. The relatively short heating time of 10 min could also partly explain the high Ce^{3+} content in the product. In general, Ce^{3+} species in CeO_{2-x} are easily oxidized to Ce^{4+} species in oxidative atmosphere.[6,7] So, prolonged heating at high temperatures (such as 300 °C) would be expected to promote the formation of the more thermodynamically stable $Ce(IV)O_2$. Thus, we succeeded in synthesizing a CeO_2 MARIMO rich in Ce^{3+} with a very high specific surface area using a facile one-step solvothermal reaction with acetonitrile as the solvent.

According to the literature,[43] the presence of Ce^{3+} in the CeO_2 improves the low temperature activity of this material in the vapor-phase CO oxidation reaction. Consequently, the superior low temperature activity of the CeO_2-AN-tEG compared with the JRC-CEO-5 in the vapor phase (Fig. 4b) can be ascribed to the larger amount of Ce^{3+} in the former, as confirmed by the HAXPES analysis. However, in the case of the liquid-phase benzyl alcohol oxidation (Fig. 4c), Ce^{4+} on the surfaces of the CeO_2 nanocrystals played a crucial role in catalyzing the reaction by oxidizing the alcohol with the concurrent reduction of Ce^{4+} to Ce^{3+}. The valence change from Ce^{3+} to Ce^{4+} in this catalytic cycle is not as pronounced when using the CeO_2-AN-tEG, because it has more Ce^{3+} contents. Thus, a longer time span is required for Ce^{3+} in this material to be oxidized by atmospheric O_2 to Ce^{4+} prior to the benzyl alcohol oxidation. In fact, the induction period was reduced by 48 h pre-treatment of CeO_2-AN-tEG under O_2 prior to liquid-phase catalytic reaction (Fig. S6a†). In addition, the induction period was found to disappear when calcined CeO_2-AN-tEG was used as a catalyst (Fig. S6a†), which mostly composed of Ce^{4+} species (Fig. S6b†). The BET specific surface area of 127 m^2 g^{-1} and the BJH pore size less than 2.43 nm (the lower limit of the instrument) in the calcined CeO_2-AN-tEG were almost same to those of as-synthesized CeO_2-AN-tEG. Therefore, absence of the induction period was due to difference of an electronic state of CeO_2 instead of its structure.

As for the solvents for CeO_2 synthesis, when a methanol solution is heated to 300 °C, the condensation of methanol would be expected to produce dimethyl ether and H_2O. The resulting H_2O would accelerate the hydrolysis of $Ce(NO_3)_3\cdot 6H_2O$ to yield CeO_2 *via* $Ce(OH)_4$, and the increased crystal size would in turn increase the Ce^{4+} concentration in the CeO_2 nanocrystals. Consequently, we propose that the suppression of H_2O formation from methanol during the solvothermal reaction could be an additional reason for the high Ce^{3+}

Table 1 Synthetic conditions used to obtain ceria porous spheres

Sample name[a]	Solvent	Additive	Temperature (°C)
CeO_2-AN-tEG	CH_3CN	Triethylene glycol	300
CeO_2-AN7-W3-tEG	$CH_3CN/H_2O = 7/3$ (v/v)	Triethylene glycol	250[b]
CeO_2-AN5-W5-tEG	$CH_3CN/H_2O = 5/5$ (v/v)	Triethylene glycol	250[b]
CeO_2-W-tEG	H_2O	Triethylene glycol	250[b]

[a] AN, tEG and W indicate acetonitrile, triethylene glycol and water, respectively. [b] Diffraction peaks ascribed to a non-cubic ceria phase were recognized in the XRD patterns of the product obtained at 300 °C (Fig. S7), so that the reaction temperature was lowered to 250 °C (Fig. S8).

concentration in the CeO_2. Then, we selected an aprotic polar solvent (acetonitrile) instead of methanol in expectation of no H_2O formation at elevated temperature. To test our hypothesis, mixtures of acetonitrile and H_2O were applied as the reaction media in solvothermal reaction trials (Table 1). The crystallite sizes were found to increase in proportion to the amount of water in the reaction solution (Table S3† and Fig. 6a), which indicates that water does indeed accelerate crystal growth. Fig. 6b presents the HAXPES profiles normalized by the peak intensities at the position of a Ce^{4+} peak (883.0 eV). As expected, the peak intensities at 885.2 and 903.4 eV ascribed to Ce^{3+} species strengthened as the water level in the reaction solvent decreased. Thus, the Ce^{3+}/Ce^{4+} ratio in the CeO_2 MARIMO could be readily adjusted by varying the water/acetonitrile ratio. In addition, XRD peak shifted to lower angles with increasing acetonitrile ratio in acetonitrile/water mixed solvents (Fig. S9†). The result indicates lattice expansion of cubic CeO_2, where increasing amounts of Ce^{3+} cation with larger ionic radius than that of Ce^{4+} cation would expand lattice size of CeO_2 crystallites.[17,44] The peak fitting curves of HAXPES spectra were showed in Fig. S10,† and the details of the crystallite sizes, the calculated Ce^{3+} concentrations in the CeO_2 and lattice parameter are summarized in Tables S2 and S3.†

Oxygen storage capacity

Ceria has been recognized as one of the best materials for oxygen storage and transfer in catalytic systems.[5,11–13] As an example, the Ce^{3+}/Ce^{4+} cycling phenomenon has been applied to the catalytic treatment of automobile exhaust gases. There has also been much effort devoted to obtaining higher concentrations of Ce^{3+} in CeO_2 catalysts so as to enhance the oxygen transfer process. Based on the HAXPES data, the CeO_2-AN-tEG was expected to exhibit exceptional OSC, and this was evaluated by cyclic O_2-pulse measurements at 200 and 400 °C (Fig. 7). The reference material JRC-CEO-5 demonstrated an OSC of approximately 22 μmol-O g^{-1} during five cycles at 200 °C (Fig. 7a), whereas the CeO_2-AN-tEG showed a much larger value of 232 μmol-O g^{-1} during the first cycle at 200 °C. However, this high OSC abruptly decreased to quite a low value of approximately 11 μmol-O g^{-1} on subsequently cycling. The initial large OSC is attributed to the high concentration of oxygen defects originally associated with Ce^{3+} ions in the material. The subsequent drop in the OSC value is believed to have resulted from the insufficient reduction of the CeO_2 by H_2 at the low temperature of 200 °C. For this reason, reduction temperatures of CeO_2-AN-tEG and JRC-CEO-5 were investigated by H_2-TPR. Fig. S11† showed that reduction of CeO_2-AN-tEG and JRC-CEO-5 started at 250 °C and 350 °C, respectively. Then, additional
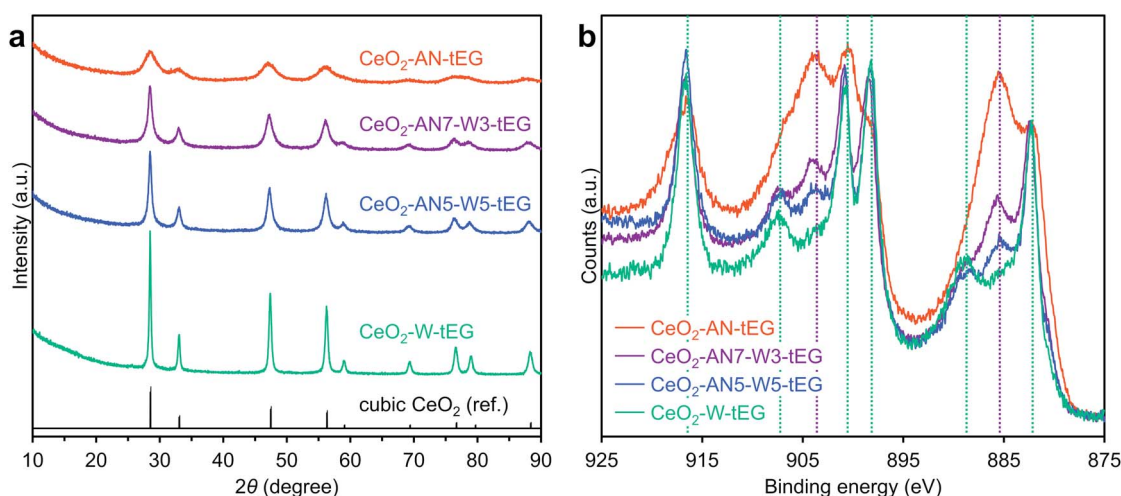

Fig. 6 (a) XRD patterns of CeO_2-AN-tEG, CeO_2-AN7-W3-tEG, CeO_2-AN5-W5-tEG and CeO_2-W-tEG. Black line represents reference XRD pattern of cubic CeO_2. (b) Ce 3d HAXPES spectra of CeO_2-AN-tEG, CeO_2-AN7-W3-tEG, CeO_2-AN5-W5-tEG and CeO_2-W-tEG. Green and purple lines show peak positions of Ce^{4+} and Ce^{3+}, respectively.
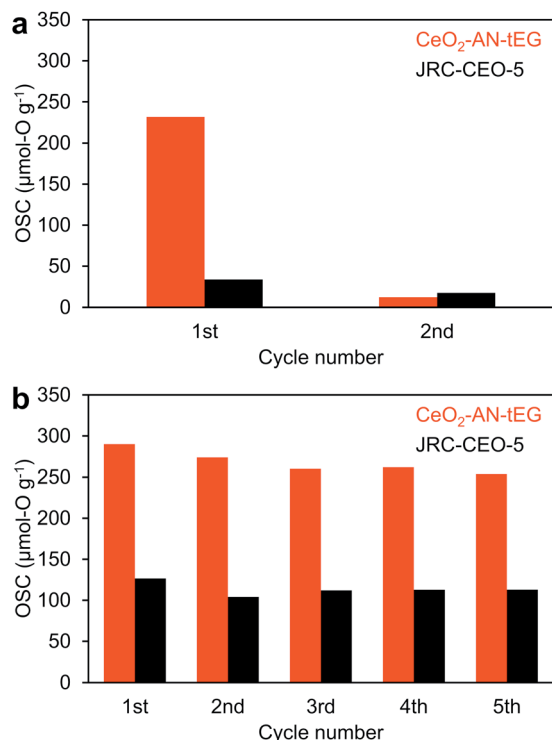
Fig. 7 Oxygen storage capacity of CeO$_2$-AN-tEG (red) and JRC–CEO-5 (black) measured by cyclic O$_2$-pulse measurements at (a) 200 °C and (b) 400 °C.

cyclic O$_2$-pulse measurements were performed at 400 °C, and the OSC values for the JRC-CEO-5 and CeO$_2$-AN-tEG were found to be 114 and 268 μmol-O g^{-1}, respectively (Fig. 7b). Unlike the result obtained at 200 °C, small changes (less than 12.4% decreasing) of these OSC values were observed during 5 cycles. The enhanced durability of the OSC value can be explained by a larger amount of oxygen defect generated by higher temperature reduction at 400 °C as illustrated in Fig. S12.† Importantly, the OSC value for the CeO$_2$-AN-tEG was two times larger than that for the JRC-CEO-5. Interestingly, the specific surface areas of the JRC-CEO-5 and CeO$_2$-AN-tEG before cyclic O$_2$-pulse measurements at 400 °C (after calcination at 400 °C for 1 h in air) were 86 and 78 m^2 g^{-1}, respectively. Thus, although the specific surface area of CeO$_2$-AN-tEG was smaller a little bit than that of JRC-CEO-5, this material exhibited a high OSC, and so these results are ascribed to the improved diffusion of oxygen in the CeO$_2$-AN-tEG nanocrystals.

Conclusions

A simple one-pot single-step solvothermal method using acetonitrile as a solvent and triethylene glycol as an additive produced porous ceria with a monodisperse spherical morphology. Compared with reference CeO$_2$, the porous spheres generated in this work showed high performance not only as a catalyst support but also as a catalyst in the CO oxidation reaction. A high Ce^{3+} concentration in this material was confirmed by HAXPES at the SPring-8 facility. The superior performance of these porous CeO$_2$ spheres during the CO

oxidation reaction and their OSC of 268 μmol-O g^{-1} g at 400 °C are both attributed to the high concentration of Ce^{3+} species in this material.

Author contributions

Ayano Taniguchi: conceptualization, data curation, formal analysis, investigation, methodology, visualization, writing – original draft, writing – review & editing. Yoshitaka Kumabe: data curation, formal analysis, investigation, writing – review & editing. Kai Kan: investigation, supervision, writing – review & editing. Masataka Ohtani: conceptualization, funding acquisition, methodology, project administration, resources, supervision, writing – review & editing. Kazuya Kobiro: funding acquisition, project administration, resources, supervision, writing – review & editing.

Conflicts of interest

There are no conflicts to declare.

Acknowledgements

References

1 T. Montini, M. Melchionna, M. Monai and P. Fornasiero, *Chem. Rev.*, 2016, **116**, 5987–6041.

2 H.-H. Liu, Y. Wang, A.-P. Jia, S.-Y. Wang, M.-F. Luo and J.-Q. Lu, *Appl. Surf. Sci.*, 2014, **314**, 725–734.

3 Q. Xie, H. Zhang, J. Kang, J. Cheng, Q. Zhang and Y. Wang, *ACS Catal.*, 2018, **8**, 4902–4916.

4 J. Xu, Y. Zhang, Y. Liu, X. Fang, X. Xu, W. Liu, R. Zheng and X. Wang, *Eur. J. Inorg. Chem.*, 2019, 183–194.

5 P. Li, X. Chen, Y. Li and J. W. Schwank, *Catal. Today*, 2019, **327**, 90–115.

6 Y. Namai, K. Fukui and Y. Iwasawa, *J. Phys. Chem. B*, 2003, **107**, 11666–11673.

7 J. P. Holgado, G. Munuera, J. P. Espino and A. R. Gonzalez-Elipe, *Appl. Surf. Sci.*, 2000, **158**, 164–171.

8 C. M. Hamm, L. Alff and B. Albert, *Z. Anorg. Allg. Chem.*, 2014, **640**, 1050–1053.

9 T. Naganuma and E. Traversa, *Nanoscale*, 2012, **4**, 4950–4953.

10 J. Lu, S. Asahina, S. Takami, A. Yoko, G. Seong, T. Tomai and T. Adschiri, *ACS Appl. Nano Mater.*, 2020, **3**, 2346–2353.

11 Y. Ishikawa, M. Takeda, S. Tsukimoto, K. S. Nakayama and N. Asao, *Adv. Mater.*, 2016, **28**, 1467–1471.

12 D. Wang, Y. Kang, V. Doan-Nguyen, J. Chen, R. Küngas, N. L. Wieder, K. Bakhmutsky, R. J. Gorte and C. B. Murray, *Angew. Chem., Int. Ed.*, 2011, **50**, 4378–4381.

13 H.-X. Mai, L.-D. Sun, Y.-W. Zhang, R. Si, W. Feng, H.-P. Zhang, H.-C. Liu and C.-H. Yan, *J. Phys. Chem. B*, 2005, **109**, 24380–24385.

14 D. Devaiah, T. Tsuzuki, C. U. Aniz and B. M. Reddy, *Catal. Lett.*, 2015, **145**, 1206–1216.

15 B. M. Reddy and A. Khan, *Catal. Surv. Asia*, 2005, **9**, 155–171.

16 Y. Zhu, G. Seong, T. Noguchi, A. Yoko, T. Tomai, S. Takami and T. Adschiri, *ACS Appl. Energy Mater.*, 2020, **3**, 4305–4319.

17 X. Hao, A. Yoko, C. Chen, K. Inoue, M. Saito, G. Seong, S. Takami, T. Adschiri and Y. Ikuhara, *Small*, 2018, **14**, 1802915.

18 P. Wang, K. Ueno, H. Takigawa and K. Kobiro, *J. Supercrit. Fluids*, 2013, **78**, 124–131.

19 E. K. C. Pradeep, T. Habu, H. Tooriyama, M. Ohtani and K. Kobiro, *J. Supercrit. Fluids*, 2015, **97**, 217–223.

20 H. T. T. Nguyen, T. Habu, M. Ohtani and K. Kobiro, *Eur. J. Inorg. Chem.*, 2017, 3017–3023.

21 F. Duriyasart, A. Irizawa, K. Hayashi, M. Ohtani and K. Kobiro, *ChemCatChem*, 2018, **10**, 3392–3396.

22 B. Liu, B. Liu, Q. Li, Z. Li, R. Liu, X. Zou, W. Wu, W. Cui, Z. Liu, D. Li, B. Zou, T. Cui and G. Zou, *J. Alloys Compd.*, 2010, **503**, 519–524.

23 D. Sun, M. Gu, R. Li, S. Yin, X. Song, B. Zhao, C. Li, J. Li, Z. Feng and T. Sato, *Appl. Surf. Sci.*, 2013, **280**, 693–697.

24 C. Slostowski, S. Marre, O. Babot, T. Toupance and C. Aymonier, *Langmuir*, 2014, **30**, 5965–5972.

25 J. Papavasiliou, A. Paxinou, G. Słowik, S. Neophytides and G. Avgouropoulos, *Catal*, 2018, **8**, 544–563.

26 P. Wang and K. Kobiro, *Chem. Lett.*, 2012, **41**, 264–266.

27 C. Ho, J. C. Yu, T. Kwong, A. C. Mak and S. Lai, *Chem. Mater.*, 2005, **17**, 4514–4522.

28 M. Ohtani, T. Muraoka, Y. Okimoto and K. Kobiro, *Inorg. Chem.*, 2017, **56**, 11546–11551.

29 E. K. C. Pradeep, M. Ohtani, T. Kawaharamura and K. Kobiro, *Chem. Lett.*, 2017, **46**, 940–943.

30 H. T. T. Nguyen, Y. Kumabe, S. Ueda, K. Kan, M. Ohtani and K. Kobiro, *Appl. Catal., A*, 2019, **577**, 35–43.

31 *Japan Reference Catalyst*, https://www.shokubai.org/com/sansyo/ceria.html, accessed June 2020.

32 S. Song, X. Wang and H. Zhang, *NPG Asia Mater.*, 2015, **7**, 179–196.

33 M. Tamura and K. Tomishige, *Angew. Chem., Int. Ed.*, 2015, **54**, 864–867.

34 Z. Zhang, Y. Wang, M. Wang, J. Lü, L. Li, Z. Zhang, M. Li, J. Jiang and F. Wang, *Chin. J. Catal.*, 2015, **36**, 1623–1630.

35 J. Zhang, J. Yang, J. Wang, H. Ding, Q. Liu, U. Schubert, Y. Rui and J. Xu, *Mol. Catal.*, 2017, **443**, 131–138.

36 H. Ding, J. Yang, S. Ma, N. Yigit, J. Xu, G. Rupprechter and J. Wang, *ChemCatChem*, 2018, **10**, 4100–4108.

37 X. Ren, Z. Zhang, Y. Wang, J. Lu, J. An, J. Zhang, M. Wang, X. Wang and Y. Luo, *RSC Adv.*, 2019, **9**, 15229–15237.

38 S. Tanuma, C. J. Powellb and D. R. Penn, *Surf. Interface Anal.*, 2011, **43**, 689–713.

39 E. Bêche, P. Charvin, D. Perarnau, S. Abanades and G. Flamant, *Surf. Interface Anal.*, 2008, **40**, 264–267.

40 B. M. Reddy, A. Khan, Y. Yamada, T. Kobayashi, S. Loridant and J.-C. Volta, *J. Phys. Chem. B*, 2003, **107**, 11475–11484.

41 L. Qiu, F. Liu, L. Zhao, Y. Ma and J. Yao, *Appl. Surf. Sci.*, 2006, **252**, 4931–4935.

42 K. I. Maslakov, Y. A. Teterin, A. J. Popel, A. Y. Teterin, K. Y. Ivanov, S. N. Kalmykov, V. G. Petrov, P. K. Petrov and I. Farnan, *Appl. Surf. Sci.*, 2018, **448**, 154–162.

43 J. Li, Z. Zhang, Z. Tian, X. Zhou, Z. Zheng, Y. Ma and Y. Qu, *J. Mater. Chem. A*, 2014, **2**, 16459–16466.

44 L. Chen, P. Fleming, V. Morris, J. D. Holmes and M. A. Morris, *J. Phys. Chem. C*, 2010, **114**, 12909–12919.